Photonics **2015**, *2*, 916-932; doi:10.3390/photonics2030916

OPEN ACCESS

photonics

ISSN 2304-6732

www.mdpi.com/journal/photonics

Article

Characteristics of the Current-Controlled Phase Transition of VO_2 Microwires for Hybrid Optoelectronic Devices

Arash Joushaghani [1], Junho Jeong [1], Suzanne Paradis [2], David Alain [2], J. Stewart Aitchison [1] and Joyce K.S. Poon [1,*]

[1] Department of Electrical and Computer Engineering, University of Toronto, 10 King's College Road, Toronto, ON M5S 3G4, Canada; E-Mails: arashj@gmail.com (A.J.); dave.jeong@mail.utoronto.ca (J.J.); stewart.aitchison@utoronto.ca (J.S.A.)

[2] Defence Research and Development Canada-Valcartier, 2459 de la Bravoure Road, Quebec, QC G3J 1X5, Canada; E-Mails: suzanne.paradis@drdc-rddc.gc.ca (S.P.); david.alain@drdc-rddc.gc.ca (D.A.)

* Author to whom correspondence should be addressed; E-Mail: joyce.poon@utoronto.ca; Tel.: +1-416-978-5465.

Received: 15 August 2015 / Accepted: 25 August 2015 / Published: 28 August 2015

Abstract: The optical and electrical characteristics of the insulator-metal phase transition of vanadium dioxide (VO_2) enable the realization of power-efficient, miniaturized hybrid optoelectronic devices. This work studies the current-controlled, two-step insulator-metal phase transition of VO_2 in varying microwire geometries. Geometry-dependent scaling trends extracted from current-voltage measurements show that the first step induced by carrier injection is delocalized over the microwire, while the second, thermally-induced step is localized to a filament about 1 to 2 µm wide for 100 nm-thick sputtered VO_2 films on SiO_2. These effects are confirmed by direct infrared imaging, which also measures the change in optical absorption in the two steps. The difference between the threshold currents of the two steps increases as the microwires are narrowed. Micron- and sub-micron-wide VO_2 structures can be used to separate the two phase transition steps in photonic and electronic devices.

Keywords: optical materials; phase transition; hybrid photonics

---

1. Introduction

Shrinking the size of optoelectronic devices is attractive for increasing integration density and lowering the power consumption, often with the benefit of increased operation bandwidths because of reduced capacitances and transit times. A difficulty is that as the active volume for light-matter interaction is reduced, the transfer characteristics of the device, such as the extinction ratio (in the case of modulators and switches) or responsivity (in the case of photodetectors), tend to deteriorate. High index contrast waveguides, microcavities and plasmonics confine light in the transverse and longitudinal directions to boost the strength of the light-matter interaction. Nonetheless, because the changes in the real and imaginary parts of the refractive index of conventional optical materials (e.g., silicon, germanium, compound semiconductors, lithium niobate) tend to only be of the order of 10^{-3} to 10^{-2}, through, for example, the free carrier plasma dispersion effect, the Franz–Keldysh effect, the quantum confined Stark effect or nonlinear susceptibility (χ^2), incorporating novel materials with giant (e.g., of order unity), electronically-modifiable changes to their optical constants into integrated photonic platforms opens the opportunity for highly miniaturized optoelectronic devices.

A particularly interesting material is the correlated electron material, vanadium dioxide (VO_2). VO_2 undergoes a reversible structural reconfiguration when heated beyond the transition temperature of $T_{\mathrm{I}\to\mathrm{M}} = 340$ K [1,2] that results in an insulator-metalphase transition, decreases the resistivity by up to five orders of magnitude and increases infrared optical absorption by about one order of magnitude [3]. These remarkable changes in the electrical and optical properties are attractive for micro- and nano-scale devices [4–8], such as electronic [9,10] and optical switches [11–19]. The phase transition in VO_2 thin films can also be initiated by other external stimuli [20–22], such as applied electric fields [23,24] or currents [25], which may result in an electronic transition instead of a structural one. A transition initiated by electron injection can potentially occur on a picosecond time scale [26,27], which is suitable for high-speed electronic and photonic switching.

However, because the optical absorption of VO_2 in the insulator phase in the telecommunication wavelength range is high (e.g., the imaginary part of the refractive index of our films varies from about 0.41 at 1300 nm to 0.34 at 1650 nm [28]), VO_2 should be hybridized with low loss waveguides in photonic applications. We have recently demonstrated a hybrid silicon (Si)-VO_2 electro-absorption optical modulator/switch that is wavelength-sized in all three spatial dimensions [11]. An extinction ratio of 12 dB was achieved in the C-band for a device length of only 1 μm, while incurring an insertion loss of about 5 dB. The result set a record for the extinction ratio per length for an integrated waveguide switch. The device schematic is shown in Figure 1, and the device consisted of a (sub-)micron wide strip of VO_2 integrated on top of a 220 nm-thick Si rib waveguide. This geometry can be integrated with standard silicon-on-insulator (SOI) photonic platforms. To achieve the performance in [11] and to understand the operation possibilities and trade-offs of hybrid VO_2 optoelectronic devices require details on the characteristics of the phase transition in VO_2 micro- and nano-wires. Due to the variability in film deposition and the inchoate fabrication of VO_2 micro-/nano-structures, experiments have reported different causes and mechanisms for the phase transition, with evidence independently supporting Joule heating [29] and electronic effects [25,30,31] as the dominant causes of the phase transition. In previous experiments on electronically-induced switching, even minute leakage currents in the VO_2 can raise the

local temperature beyond $T_{I \to M}$ to induce a thermal phase transition [32]. Efforts to suppress the leakage current using high-k dielectrics [31,33,34] have generally failed to induce a conclusive phase transition at low current levels.

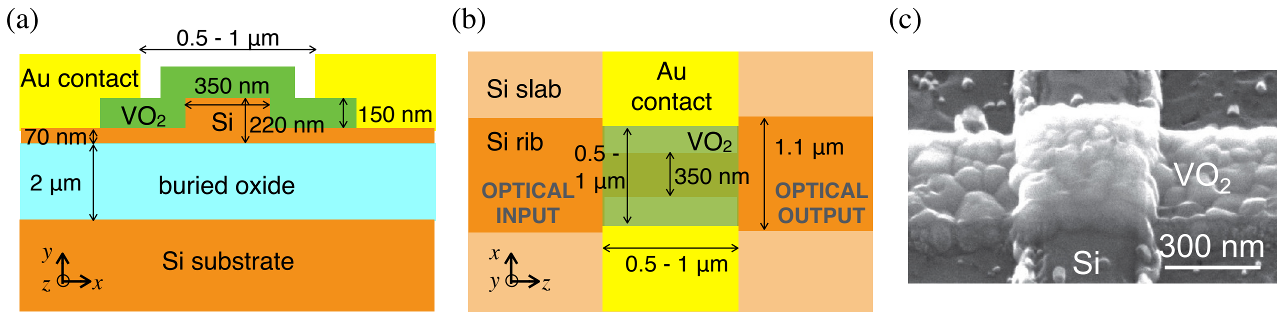

Figure 1. (**a**) The cross-section and (**b**) top views of the wavelength-sized hybrid Si-VO_2 electro-absorption switch and photodetector presented in [11]. (**c**) A scanning electron micrograph of an etched VO_2 strip atop a Si rib waveguide. This would form the active region of an electro-absorption switch/modulator.

In this article, we present geometry-dependent scaling trends from current-voltage measurements of etched VO_2 microwires that are confirmed by thermal models and infrared optical imaging to study independently each step of the two-step phase transition in VO_2. The optical and electrical properties of each transition can be used to design hybrid optoelectronic devices for switching, modulation and detection applications. In contrast to and complementing recent works to study the role of thermal effects in the electronically-induced phase transition in VO_2 [32,35] and radio frequency measurements of VO_2 strips integrated into coplanar waveguides [36], this work primarily uses DC electrical measurements of etched VO_2 microwires with a range of geometries to infer different mechanisms for each step of the phase transition. The measurements show that the first step is a carrier-induced phase transition between the insulating (I) and an intermediary, partially-metallic phase (M^*) that results in a delocalized change in the optical absorption and resistivity with almost no hysteresis; the second step is a thermally-induced phase transition to the metallic phase (M) that exhibits a wide hysteresis and is due to Joule heating as a result of current filamentation. The first transition has a smaller hysteresis and is expected to occur on a shorter time scale, which makes it suitable for optical modulation applications requiring high operation speeds and small hysteresis. Additionally, a small hysteresis allows the devices to operate with a smaller swing voltage, if they are biased close to the phase transition point. In contrast, the second transition is suitable for achieving the maximum extinction ratio.

Although the current-induced two-step phase transition in VO_2 has been previously observed [35,37], the nature of each transition was not clarified, and geometrical control over the transition thresholds was not established. Recent experiments have shown that charge injection can cause VO_2 to be in a partially-metallic phase without any structural change [32] (or the "mixed-phase" in [38]). We infer that the first transition observed here would correspond to this effect, while the change to the tetragonal crystalline structure in the metallic phase would occur in the second transition. The optical infrared imaging results presented here are also the first report of measured absorption changes after the first transition. Overall, this work helps to understand the causes of the phase transition in VO_2 and

provides guidelines for the geometry of VO_2 devices to achieve efficient and/or high-speed optical and electronic switching.

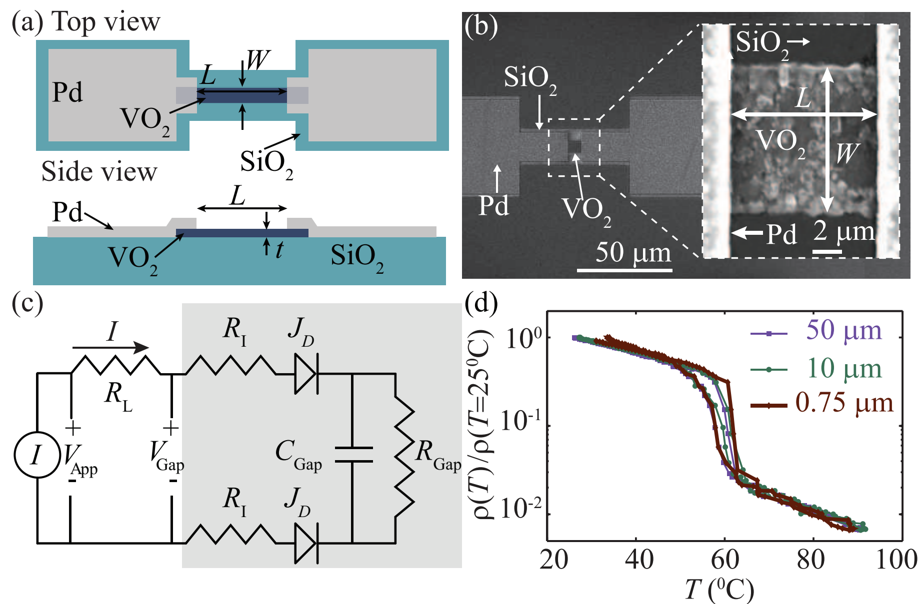

Figure 2. (**a**) The top and side view schematics of a VO_2 lateral junction. (**b**) A scanning electron micrograph of the device and (inset) the magnified image of the gap. (**c**) The equivalent circuit model of the device in the experiment. (**d**) The normalized resistivity of different microwires measured as the substrate temperature, T, for $W = 5$ µm and $L = 750$ nm, 10 µm and 50 µm.

2. Fabrication and Device Geometry

VO_2 microwires, as illustrated in Figure 2a, were fabricated using electron-beam (e-beam) lithography and reactive ion etching of a 100 nm-thick VO_2 film that was sputtered on a 2 µm-thick thermally-grown silica (SiO_2) on a silicon (Si) substrate [12]. The grain sizes of the samples, as measured using scanning electron microscopy, were about 75 ± 25 nm. Lateral electrical contacts were defined using aligned e-beam lithography followed by e-beam evaporation and lift-off of a 100 nm-thick palladium (Pd) film. The contacts were separated by a gap of length L, which varied between 0.15 µm and 7.5 µm. The microwire width, W, varied between 0.75 µm and 50 µm. Figure 2b shows a scanning electron micrograph of a device with $W = 5$ µm and $L = 5$ µm. Details about the sample preparation and fabrication are described in Appendix A.

A circuit model for the experiments is shown in Figure 2c. A current, I, was applied to the device under test using a precision sourcemeter, and the voltage across contacts, V_{Gap}, was measured. An external resistance of $R_{\text{L}} = 1$ kΩ limited the current. The VO_2 microwire was modelled as a resistance, R_{Gap}, in parallel with a capacitance, C_{Gap} [33]. The interface between the VO_2 and a Pd contact was modelled as a contact and an interface sheet resistance, R_{I}, as well as a Schottky diode (due to the work function mismatch between Pd and VO_2) with current density J_{D} [39]. This simple circuit model is useful for predicting the total resistance of the etched VO_2 microwires as described in Appendix B2. The model also shows that for the dimensions studied here, the VO_2 microwires had essentially the same material properties as the bulk film, which were not affected by the etching. This is further confirmed by

the measurements of the resistivity, $\rho = R_{Gap}Wt/L$, as a function of the substrate temperature. As an example, Figure 2d shows the measured resistivities for microwires with $W = 5$ µm and $L = 750$ nm, 10 µm and 50 µm. The transition temperature and normalized resistivity were independent of L and W, indicating that devices of this size can be modelled by the bulk material properties of VO_2.

3. Current-Induced Phase Transition

By controlling the current applied to a microwire, a two-step phase transition could be clearly observed. As an example, Figure 3a shows the measured V_{Gap} as a function of I for the $W = 10$ µm and $L = 5$ µm device. The arrows in the figure trace V_{Gap}, and the shaded regions highlight the different VO_2 phases at each current range. The drop in V_{Gap} was a direct manifestation of the phase transition and occurred in two steps. The first transition from the insulating to a partially-metallic phase (I→M*) occurred at a current $I_{I \to M^*}$ and voltage $V_{I \to M^*}$ with a narrow hysteresis width. The second transition from the partially-metallic phase to the metallic phase (M*→M) occurred at a current $I_{M^* \to M} > I_{I \to M^*}$, voltage $V_{M^* \to M} < V_{I \to M^*}$ and exhibited a wider hysteresis loop.

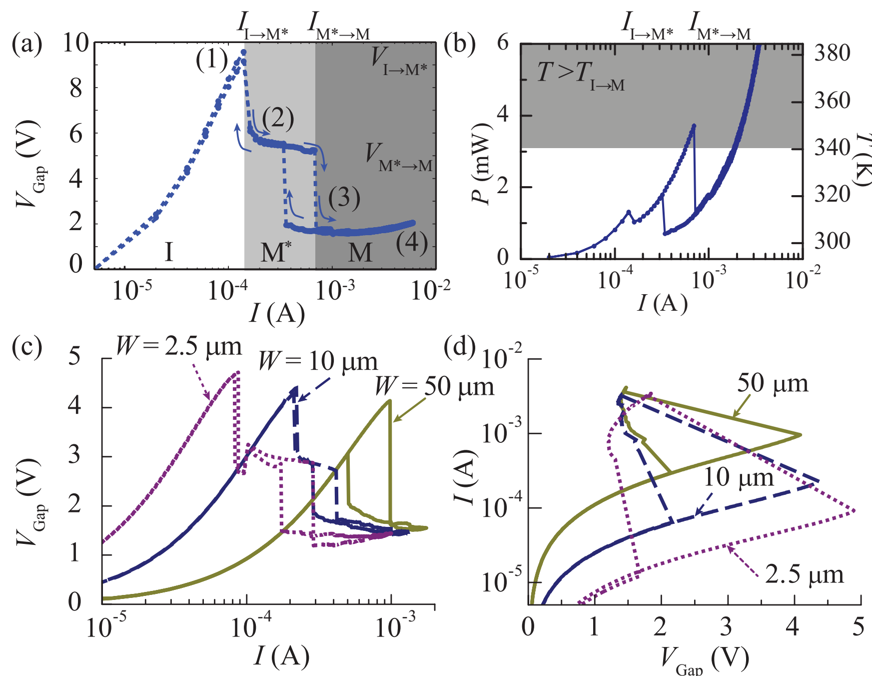

Figure 3. The (**a**) voltage-current and (**b**) power-current relationship of a the VO_2 wire with $L = 5$ µm and $W = 10$ µm. The expected temperature of the VO_2 is included in the right axis. (**c**) The voltage-current and (**d**) current-voltage relationship of a the VO_2 wire with $L = 1.25$ µm and $W = 2.5$ µm, 10 µm and 50 µm.

To determine the thermal contribution to each transition, we first simulated using a finite element method (COMSOL Multiphysics) the maximum temperature in the VO_2 during the two-step transition by taking the measured dissipated electrical power, $P = I \times V_{Gap}$, as a Joule heat source (see Appendix B1 for details). Figure 3b shows P (left axis) and the simulated temperature, T, (right axis) of the VO_2 slab, as a function of I. T was less than $T_{I \to M}$ at the first transition and reached $T_{I \to M}$ just before the second transition. These results strongly suggest that the second transition is thermally induced and results in a

fully-metallic phase, while the first transition is of a different physical origin due to the applied currents and results in a partially-metallic phase.

The current thresholds, $I_{\mathrm{I}\to\mathrm{M}^*}$ and $I_{\mathrm{M}^*\to\mathrm{M}}$, strongly depended on the geometry of the wire. As an example, Figure 3c shows the VI characteristics of three different wires with $L = 1.25$ μm and different widths of $W = 2.5$ μm, 10 μm and 50 μm. As W increased, both $I_{\mathrm{I}\to\mathrm{M}^*}$ and $I_{\mathrm{M}^*\to\mathrm{M}}$ increased, but at different rates, indicating that the two transitions were differently affected by the wire geometry. When $L = 1.25$ μm and $W \geq 50$ μm, the two transition thresholds almost overlapped and appeared almost as a single transition from the I to M phase. The two-step phase transition only occurred when the current was regulated. Figure 3d shows the IV characteristics of the devices of Figure 3c, when a voltage source swept V_{Gap}. For all devices, only a single transition was observed. If the current was not controlled, a reduction in the resistance (e.g., caused by any carrier effects) would draw more current, thereby heating the device and initiating any thermally-driven step(s) in the phase transition. Therefore, to study the two-step phase transition, it is essential to regulate the current throughout the phase transition.

3.1. Critical Electric Fields

To investigate the origin of the each transition, we examined the electric field, current and power dissipation of devices with varying widths and lengths. From the measured $V_{\mathrm{I}\to\mathrm{M}^*}$ and $V_{\mathrm{M}^*\to\mathrm{M}}$ of microwires with different lengths, we determined the "average" electric fields in the gap for the first ($E_{\mathrm{I}\to\mathrm{M}^*}$) and second ($E_{\mathrm{M}^*\to\mathrm{M}}$) phase transitions from the slopes of the transition voltages *vs*. length L (at each width, W). Figure 3a shows that $E_{\mathrm{I}\to\mathrm{M}^*}$ and $E_{\mathrm{M}^*\to\mathrm{M}}$ were roughly constant and were approximately 12 ± 1 kV/cm and 6 ± 1 kV/cm, respectively. The field transition thresholds were independent of the wire geometry and were intrinsic properties of the VO_2. Although $E_{\mathrm{I}\to\mathrm{M}^*}$ was roughly constant with W, $V_{\mathrm{I}\to\mathrm{M}^*}$ varied significantly with W (for the same L) due to the VO_2-Pd interface resistance. The effect of the interface is well modelled by the circuit in Figure 2 and described in Appendix B2. The interface resistance was a result of electron scattering and the work function mismatch. The interface resistance increased with decreasing W and resulted in higher values of $V_{\mathrm{I}\to\mathrm{M}^*}$.

From the $V_{\mathrm{I}\to\mathrm{M}^*}$ and $V_{\mathrm{M}^*\to\mathrm{I}}$ *vs*. L relations, we extrapolated the offset voltages of the transition voltages, *i.e.*, the transition voltages as $L \to 0$, as shown in Figure 4b. V_0 decreased with increasing W for the first transition, as expected from decreasing the interface resistance. The second transition had a lower V_0 since the resistivity of the VO_2 had been reduced by about one order of magnitude after the first transition. Interestingly, V_0 for the second transition was nearly independent of W, suggesting that the second phase transition was spatially localized to a width less than W. Filamentation is a signature of a thermally-induced transition in VO_2 [40], which is accompanied by a structural phase transition [29].

3.2. Threshold Current Densities

The different mechanisms behind the two phase transitions are further manifested in the device geometry dependence of the currents, $I_{\mathrm{I}\to\mathrm{M}^*}$ and $I_{\mathrm{M}^*\to\mathrm{M}}$, and dissipated power, $P_{\mathrm{I}\to\mathrm{M}^*}$ and $P_{\mathrm{M}^*\to\mathrm{M}}$, at the phase transitions. Figure 4c,d shows that, unlike the transition electric fields, $I_{\mathrm{I}\to\mathrm{M}^*}$ and $I_{\mathrm{M}^*\to\mathrm{M}}$ exhibited scaling trends with W. $I_{\mathrm{I}\to\mathrm{M}^*}$ increased almost linearly with W, and we extrapolated a threshold current

density for the first transition of $J_{\mathrm{I}\rightarrow\mathrm{M}^*} = 36 \pm 15$ kA/cm^2. This current density is related to the VO_2 carrier density, n, through the drift current relation,

$$J_1 = qn\mu_e E_{\mathrm{I}\rightarrow\mathrm{M}^*}, \tag{1}$$

where q is the elemental charge and μ_e is the VO_2 electron mobility [41], which is about 0.5 cm$^2/(\mathrm{V{\cdot}s})$. The critical carrier density for the first transition was about $n = (3.7 \pm 1.4) \times 10^{19}$ cm^{-3}. In contrast, $I_{\mathrm{M}^*\rightarrow\mathrm{M}}$ was nearly constant with W, which again implies that the second transition was spatially localized. The different dependences of $I_{\mathrm{I}\rightarrow\mathrm{M}^*}$ and $I_{\mathrm{M}^*\rightarrow\mathrm{M}}$ on W and L further emphasize the geometrical control over the two-step transition. The separation between the two transitions decreases with increasing W, and eventually, a single transition is observed when $I_{\mathrm{I}\rightarrow\mathrm{M}^*} \rightarrow I_{\mathrm{M}^*\rightarrow\mathrm{M}}$.

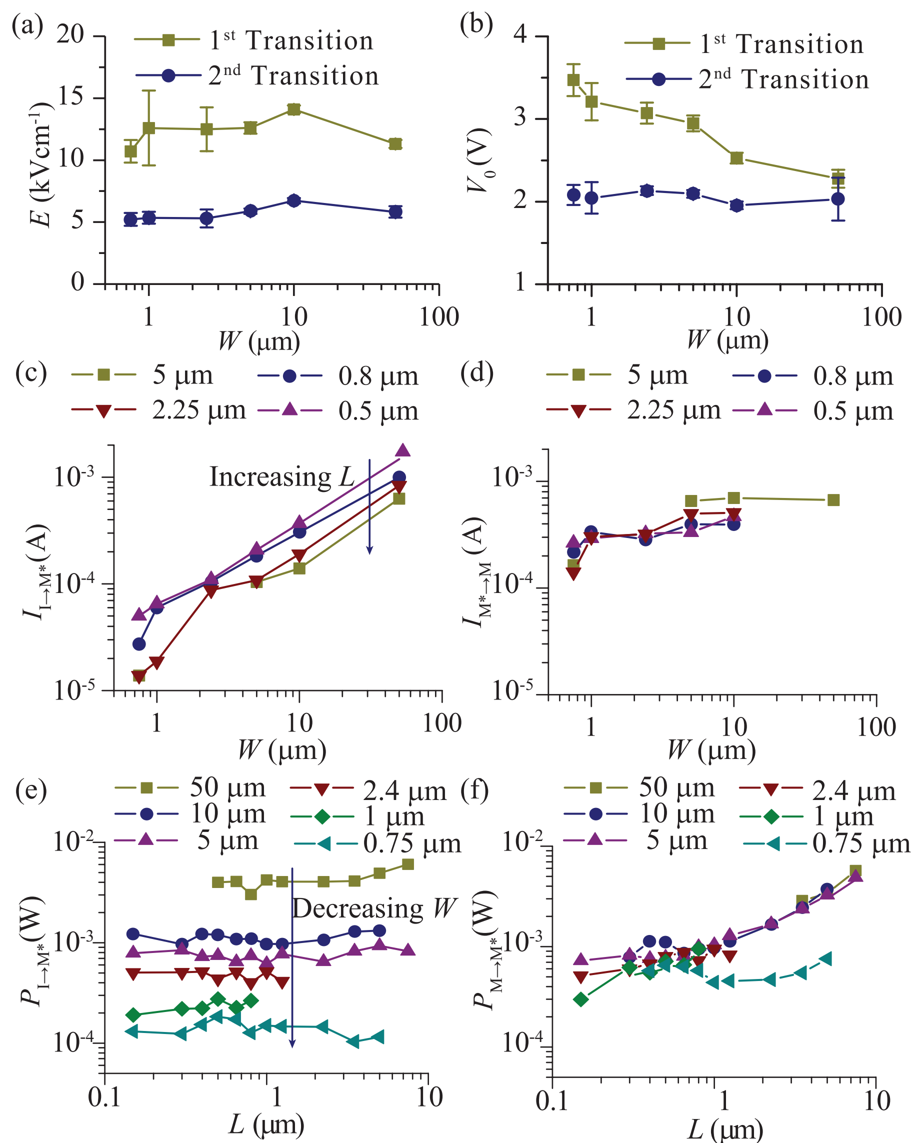

Figure 4. (**a**) The "average" electric field and (**b**) the transition voltage offset for both transitions *vs.* W. The transition currents for the (**c**) first and (**d**) second transitions as a function of W for several values of L. The dissipated power density for the (**e**) first and (**f**) second transitions as a function L for several values of W.

Figure 4e shows that $P_{\mathrm{I}\to\mathrm{M}^*}$ was essentially independent of L and only varied by $< 15\%$ over the two orders of magnitude of change in L. This is further evidence that the first transition was not thermally induced, since longer microwires would require higher powers to reach $T_{\mathrm{I}\to\mathrm{M}}$ for a thermal transition. Indeed, the second transition, $P_{\mathrm{M}^*\to\mathrm{M}}$, shown in Figure 4f, scaled linearly with L, a confirmation that the second transition was thermally induced. However, $P_{\mathrm{M}^*\to\mathrm{M}}$ had almost no dependence on W when $W \gtrsim 1$ µm, indicating that the localized filament was a few microns wide. The width of the filament is likely affected by the thermal conductivity of the substrate and the homogeneity of the VO_2 film. The distinct dependences of transition currents and dissipated electrical power on the microwire geometry, L and W, can be used to specify devices that isolate one phase transition from the other.

4. Optical Absorption

Finally, to directly visualize a delocalized electronic transition and filamentation in the thermal transition, we measured the spatial profile of the optical transmission, K, of the VO_2 microwires using an erbium-doped fibre broadband light source with a centre wavelength of 1530 nm. Since this wavelength has an energy similar to the bandgap of VO_2, it is sensitive to changes in the VO_2 near the bandgap. Previous visible light imaging experiments have reported no detectable change in the optical transmission during the first phase transition [38].

Figure 5a,b, respectively, shows the infrared (IR) and visible images of the device with $W = 10$ µm and $L = 5$ µm. Figure 5c shows the decrease in the transmission extracted from the IR images normalized to the transmission when no current is applied. The change in the transmission, ΔK, is defined as:

$$\Delta K = -\frac{K(I) - K(I \to 0)}{K(I \to 0)}. \tag{2}$$

The parenthesized numbers in Figure 5c correspond to the currents labelled in Figure 3a, and the boundaries of the VO_2 microwire are marked with white dashed lines.

Figure 5c-1 shows no detectable change in the transmission when $I < I_{\mathrm{I}\to\mathrm{M}^*}$. Figure 5c-2 shows that after the first transition, the VO_2 was in the M* phase, and ΔK increased to $1.5 \pm 0.2\%$ over the entire microwire. After the second transition, as shown in Figure 5c-3, the spatial profile of ΔK collapsed to a filament and ΔK increased to $12 \pm 0.2\%$. At this point, the filament is composed of VO_2 in its M phase. Beyond $I_{\mathrm{M}^*\to\mathrm{M}}$, as shown in Figure 5c-4, the filament width and the spatial extent of the M phase grew and ΔK increased to $22.0 \pm 0.5\%$. The change in the optical transmission, ΔK, for the two transitions as a function of W for microwires with $L = 5$ µm is summarized in Figure 5d. ΔK for the first transition was at least $10\times$ smaller than the second transition. Figure 5e shows the imaged full-width at half-maximum (FWHM) of the filament, ω, after the second transition for microwires with $L = 5$ µm. In agreement with the electric field, current and power dissipation measurements (Figure 4b,d,f), the second phase transition was spatially confined to a filament that was 1 to 2 µm wide when $W \gtrsim 1$ µm.

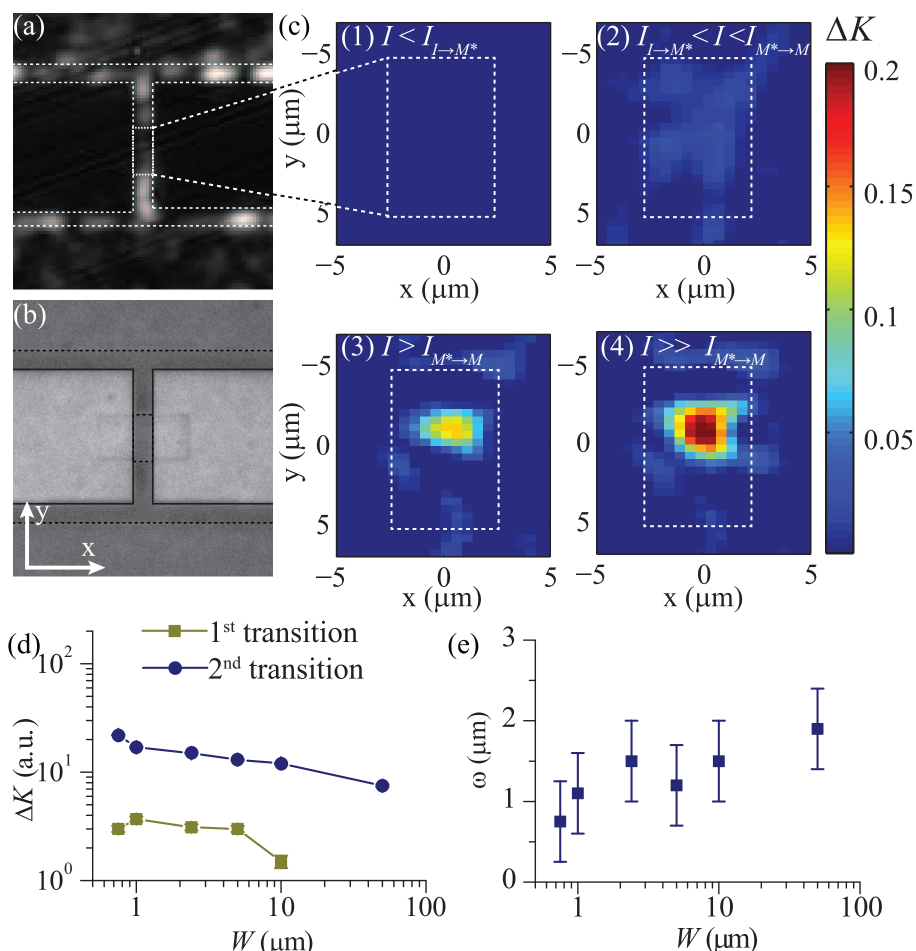

Figure 5. The (**a**) infrared and (**b**) visible optical images of the VO_2 device with $W = 10$ µm and $L = 5$ µm. (**c**) The decrease in the infrared optical transmission as the current is increased. Each sub-figure corresponds to a current labelled in Figure 3a. (**d**) The decrease in the infrared optical transmission after each transition and (**e**) the width of the filament as a function of W when $L = 5$ µm.

5. Discussion

The measurements presented here have shown that injected carriers can initiate two-step phase transition in VO_2 microwires. The threshold current to initiate the first step of the phase transition is strongly dependent on the VO_2 microwire length and width, while the second step is somewhat geometry independent down to widths of about 1 to 2 μm, because the phase transition is initially confined to a filament of this width. The two-step phase transition can appear as a single step in wide wires, when the threshold current required to reach the critical carrier density leads to heating beyond $T_{\mathrm{I \to M}}$. The difference in the threshold currents between the two steps of the phase transition can be increased by decreasing the microwire width.

These results are important for device applications. For example, for switching or modulation devices requiring the largest change in the resistivity and optical absorption, the two steps of the phase transition should be used together, though the operation speed would be limited by the slow structural transition. In addition, the VO_2 region should be designed to be narrower than the filament ($\sim$ 1 µm in our films) for optimal efficiency. The initiation of both steps of the phase transition can be readily accomplished by

sweeping the applied voltage rather than the current, since a controlled current can suppress the thermal effects that lead to the second step in the phase transition. As an example, the wavelength-sized hybrid Si-VO_2 electro-absorption waveguide optical switches implemented in [11] used these principles. The length of the VO_2 region was kept to ≤ 1 μm to maximize the efficiency, and the device was driven by an applied voltage.

By controlling the current injection, it is possible to initiate the first electronic transition only without the second thermal step, which should lead to faster devices, lower power thresholds and drastic reductions in the hysteresis. Reducing the hysteresis would reduce the amplitude of the modulation current necessary to operate the device and to lower the dynamic switching power. Current-controlled, rather than voltage-controlled VO_2 switching also leads to longer device lifetimes [37]. Moreover, since the electronic phase transition is geometry independent (the optical absorption across the entire microwire is modified), it is possible to use a wider microwire atop a waveguide to achieve the same extinction ratio as a device that uses both steps of the phase transition. However, narrower microwires have the advantage of having a larger threshold current difference between two steps of the phase transition.

6. Conclusions

In summary, we have shown through geometry-dependent scaling trends and infrared imaging that the first step in the current-induced phase transition in VO_2 is delocalized and spans the entire microwire, while the second step is confined to a 1 μm to 2 μm-wide filament. Suppressing or separating the thermal transition from the electronically-induced transition using device geometry and controlled carrier injection can potentially lead to high-speed and power-efficient electronic and optical devices. The results also show that miniaturizing VO_2 devices would have the benefit of a reduced threshold current for the phase transition, as well as an increased separation between the two steps in the phase transition.

Acknowledgements

A.J. thanks I. Sigal and R. Gad for their assistance with the optical measurements and helpful discussions. Financial support from the Natural Sciences and Engineering Research Council of Canada, Ontario Graduate Scholarship program, and the Canada Research Chair program is gratefully acknowledged. The paper is an invited contributed paper as part of the Special Issue on Hybrid and Heterogeneous Technologies in Photonics Integrated Circuits.

Author Contributions

A.J. performed the experiments and simulations. J.J. assisted A.J. in the device fabrication and electrical measurements. S.P. and D.A. deposited the VO_2 film. J.K.S.P. and J.S.A. supervised the research and provided guidance in the experiments. A.J. and J.K.S.P. analysed the data and prepared the manuscript with comments from the co-authors.

Conflicts of Interest

The authors declare no conflict of interest.

Appendix A: Experimental Details

A1. VO_2 Sputtering

VO_2 thin films were deposited by reactive radio frequency (RF) magnetron sputtering of a 50 mm vanadium target (99.7% purity). A 50 mm Si wafer with 2 μm of thermally-grown SiO_2 was placed on a 150 mm Si wafer, which was maintained at 550 °C during the deposition. High purity argon (Ar) and oxygen (O_2) were introduced in the chamber with the respective flow rates of 80.0 sccm and 2.0 sccm at a total pressure of 10 mT. The sputtering was initiated by ramping the RF power to 200 W, at which point the stoichiometry was maintained by adjusting the flow rate of O_2 to keep the DC bias of the sample at a constant value. Typical deposition rates were 0.03 nm/s. The grain sizes were not explicitly controlled during this deposition process. The average grain size for the samples used in the experiments was about 75 ± 25 nm, as determined from cross-section scanning electron micrographs.

A2. Fabrication of the Etched VO_2 Microwires

VO_2 samples were cleaned using acetone and isopropanol, dried with a nitrogen gun and baked at 80 °C for three minutes. The samples were cooled down before spinning the resist. HMDS primer and ZEP-520A were sequentially spin-coated on the VO_2 samples each for 60 s at 2000 rpm. The samples were then cured at 180 °C for 180 s and then exposed to an electron beam (e-beam) using a Vistec EBPG 5000+ system at a typical electron dose of 250 μC/cm^2 and a current of 500 pA for nano-structures and 400 μC/cm^2 and a current of 5 nA for micron-sized devices. The samples were developed in ZED-N50 for 60 s and dipped in methyl isobutyl ketone (MIBK):isopropyl alcohol (IPA) 9:1 for 15 s. The resulting resist layer was 700 nm thick with a minimum wire width of $\approx$ 75 nm. The resist was cured at 110 °C for four minutes prior to etching. The samples and the chuck were pre-heated to 80 °C just before etching to ensure that the VO_2 was etched in its metallic state. The samples were etched for 35 s in a gas mixture of Cl_2 (6 sccm), H_2 (6 sccm) and Ar (9 sccm), which was maintained at a total pressure of 5 mT and was ionized with an RF power of 100 W and an ICP power of 500 W. Longer etches were conducted sequentially in 35-s intervals with 60-s cool down periods. The cool down period ensured that the resist could be easily removed after the etching. After the etching, the resist was removed by immersion, with gradual shaking of the samples at 60 °C in the ZEP resist remover (ZDMAC) for 180 s followed by 15 s of sonication in the same solution.

The contact patterns were first transferred to ZEP-520A with the same procedure outlined above. Square gold (Au) markers at the four corners of the sample were used to align the the contacts with the microwires. Contacts were deposited using e-beam evaporation of 0.2 nm of chromium followed by 100 nm of Pd with an initial rate of 0.001 nm/s, which was slowly ramped up to 0.01 nm/s. The resist was then lifted off by sonication of samples in 40 °C ZDMAC for 180 s.

A3. Measurements

The devices were probed using tungsten needles held in DC probe positioners. The current-voltage measurements were carried out using the precision sourcemeter (Keithley Model 2636A) on a temperature-controlled stage, which controlled the temperature by adiabatically increasing the stage current to avoid temperature overshoots. The optical measurements were carried out by placing the chip on a transparent glass slide and illuminating from the bottom side of the chip. The broadband erbium-doped fibre source was JDS Uniphase OAB 1415-16-Z001 without any inputs. The transmitted light was collected from the top through a 20 times infinity-corrected long working distance objective (Mitutoyo). The IR images were captured using an InGaAs camera (Xenics XEVA Model 1324).

Appendix B. VO_2 Modelling and Simulations

For the calculations and simulations, the VO_2 properties were either experimentally measured at the metallic and insulating states or their values were extracted from the literature. The temperature dependence of those variables were then extrapolated using the line shape function, $F(T)$, which was derived by fitting the experimental values of temperature-dependent bulk resistivity, ρ, to the function:

$$\rho(T) = (\rho_{\mathrm{I}} - \rho_{\mathrm{M}})\,[1 - F(T)] + \rho_{\mathrm{M}}, \tag{B1a}$$

$$F(T) = \frac{e^{-\alpha T}}{1 + e^{\frac{T - T_C}{\Delta T}}}, \tag{B1b}$$

where $\rho_{\mathrm{I}} = 2\ \Omega\cdot\mathrm{cm}$ and $\rho_{\mathrm{M}} = 0.02\ \Omega\cdot\mathrm{cm}$ are respectively the resistivities in the insulating and metallic states of VO_2, and the $F(T)$ fitting parameters were $\alpha = 0.02\ \mathrm{K}^{-1}$, $T_C = 337$ K and $\Delta T = 2$ K.

B1. Thermal Modelling

In Figure 3b, to determine the contribution of thermal effects to each transition, we simulated the VO_2 temperature using the heat transfer module in COMSOL Multiphysics. The simulations included the three-dimensional structure of the device, which was non-uniformly meshed with a minimum mesh size of 5 nm, such that the critical dimensions in each direction included at least 10 elements. The section of the VO_2 wire between the electrodes was used as a heat source with a total power of $P = I \times V_{\mathrm{Gap}}$. The side and the bottom boundaries were set at room temperature and were sufficiently far apart to have no influence on the thermal transport properties of the wire. The top surfaces were modelled as convective cooling surfaces. The VO_2 thermal conductivity of insulating and metallic VO_2 were taken from [42] and had T line shape function $F(T)$. The heat capacity was modelled according to [40].

B2. Electrical Modelling

An electrical model of the device is shown in Figure 2c. The interface between the VO_2 and the metal is modelled as a Schottky diode with a barrier height ϕ_{B0} and a breakdown voltage V_{C}. Using this model, the IV characteristics of the diode were calculated. The Schottky barrier height between the VO_2 and the metal is $\phi_{\mathrm{B0}} = \phi_{\mathrm{m}} - \phi_{\mathrm{s}} + (E_{\mathrm{C}} - E_{\mathrm{F}})$, where ϕ_{m} and ϕ_{s} are respectively the metal and VO_2 work functions

and $E_C - E_F$ is the difference between the conduction band energy and the Fermi level of VO_2 [39]. The diode current density, J_D, is then given by:

$$J_D = J_s \left[\exp\left(\frac{qV_a}{kT}\right) - 1 \right], \tag{B2}$$

where V_a is the applied potential across the diode and J_s is the saturation current density of this diode at room temperature, which can be estimated from the thermionic emission model of an intrinsic semiconductor to be $J_s = 3.3 \times 10^4$ A/m^2 [39,43]. Equation (B2) provides an accurate description when the diode is in forward bias. The IV characteristics in reverse bias can significantly deviate from the above equation, as the VO_2-Pd diode could easily breakdown under large applied electric fields.

In the VO_2 wire, the carrier density without any applied voltages is given by $n = 1/(\rho q \mu_e)$, where $\mu_e = 0.5$ cm^2/(V·s) is the VO_2 electron mobility [41]. Using the bulk resistivity values of $\rho = 2$ Ω·cm, we estimate the carrier density to be $n = 1.25 \times 10^{18}$ cm^{-3}.

Using the above diode model, the carrier density, as well as the circuit model of Figure 2c, we can predict the resistance of VO_2 microwires with different L and W. Figure B1 shows the measured resistivity of VO_2 wires *vs.* L for several values of W, where the symbols are the measured data and the solid lines are the model calculations. The good agreement between the experimental results and calculations shows that this simple model can capture the behaviour of VO_2 at the Pd interface [39]. It should be noted, however, that the model assumes that the junction is longer than the depletion region and will be invalid when $L \leq 100$ nm.

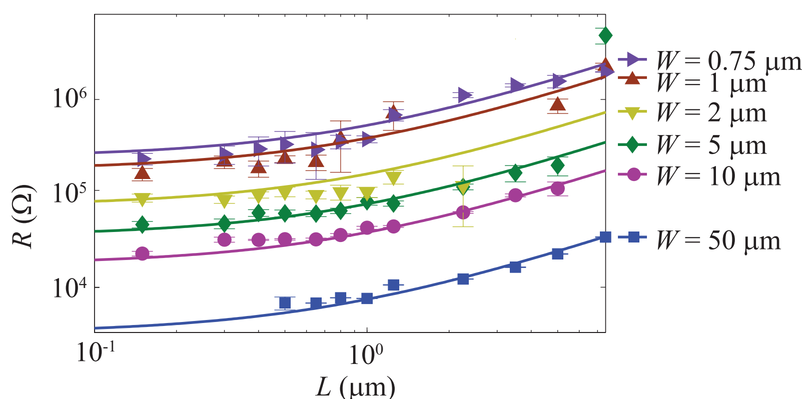

Figure B1. The measured (symbols) and calculated (solid lines) resistance of VO_2 wires as a function of L for several values wire W.

This model can also predict the resistance of the microwire in the metallic state, which occurs when the thermal filament spatially spans the whole wire (*i.e.*, $I >> I_2$). The resistance ratio of the microwires was defined as $10\log_{10}[R(I \to 0)/R(I >> I_2)]$. Figure B2a,b respectively, shows the measured and calculated resistance ratio after the phase transition. As expected, the model can predict the trends in the resistance ratio using parameters of bulk VO_2 film.

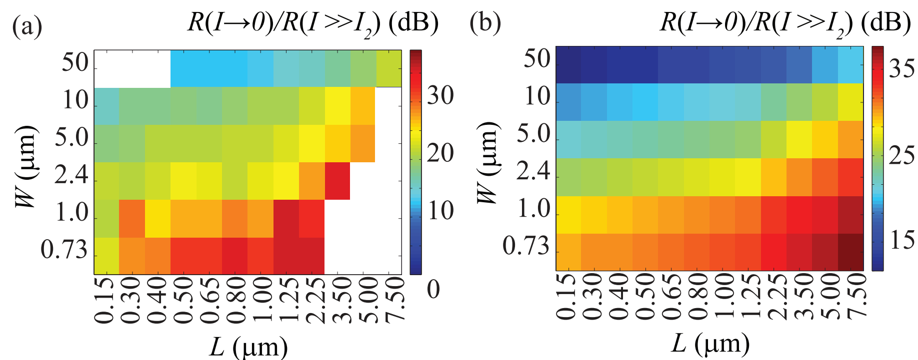

Figure B2. The (**a**) measured and (**b**) calculated change in the resistance of VO_2 wires as a function of L and W.

References

1. Morin, F.J. Oxides which show a metal-to-insulator transition at the Neel temperature. *Phys. Rev. Lett.* **1959**, *3*, 34–36.
2. Basov, D.N.; Averitt, R.D.; van der Marel, D.; Dressel, M.; Haule, K. Electrodynamics of correlated electron materials. *Rev. Mod. Phys.* **2012**, *83*, 471–541.
3. Berglund, C.N.; Guggenheim, H.J. Electronic properties of VO_2 near the semiconductor-metal transition. *Phys. Rev.* **1969**, *185*, 1022–1033.
4. Yang, Z.; Ko, C.; Ramanathan, S. Oxide electronics utilizing ultrafast metal-insulator transitions. *Annu. Rev. Mater. Res.* **2011**, *41*, 337–367.
5. Goldflam, M.D.; Driscoll, T.; Chapler, B.; Khatib, O.; Marie Jokerst, N.; Palit, S.; Smith, D.R.; Kim, B.J.; Seo, G.; Kim, H.T.; *et al.* Reconfigurable gradient index using VO_2 memory metamaterials. *Appl. Phys. Lett.* **2011**, *99*, doi:10.1063/1.3615804.
6. Bouyge, D.; Crunteanu, A.; Orlianges, J.C.; Passerieux, D.; Champeaux, C.; Catherinot, A.; Velez, A.; Bonache, J.; Martin, F.; Blondy, P. Reconfigurable bandpass filter based on split ring resonators and vanadium dioxide (VO_2) microwave switches. In Proceedings of the Asia Pacific Microwave Conference, Singapore, 7–10 December 2009; pp. 2332–2335.
7. Dicken, M.J.; Aydin, K.; Pryce, I.M.; Sweatlock, L.A.; Boyd, E.M.; Walavalkar, S.; Ma, J.; Atwater, H.A. Frequency tunable near-infrared metamaterials based on VO_2 phase transition. *Opt. Express* **2009**, *17*, 18330–18339.
8. Kats, M.A.; Sharma, D.; Lin, J.; Genevet, P.; Blanchard, R.; Yang, Z.; Qazilbash, M.M.; Basov, D.N.; Ramanathan, S.; Capasso, F. Ultra-thin perfect absorber employing a tunable phase change material. *Appl. Phys. Lett.* **2013**, *101*, doi:10.1063/1.4767646.
9. Walden, R.H. Two switching devices utilizing VO_2. *IEEE Trans. Elec. Dev.* **1970**, *17*, 603–612.
10. Martens, K.M.; Radu, I.P.; Rampelberg, G.; Verbruggen, J.; Cosemans, S.; Mertens, S.; Shi, X.; Schaekers, M.; Huyghebaert, C.; De-Gendt, S.; *et al.* VO_2: A metal-insulator transition material for nanoelectronic applications. *ECS Trans.* **2012**, *45*, 151–158.
11. Joushaghani, A.; Jeong, J.; Paradis, S.; Alain, D.; Aitchison, J.S.; Poon, J.K.S. Wavelength-size hybrid Si-VO_2 waveguide electro-absorption optical switches and photodetectors. *Opt. Express* **2015**, *23*, 3657–3668.

12. Joushaghani, A.; Kruger, B.A.; Paradis, S.; Alain, D.; Stewart Aitchison, J.; Poon, J.K.S. Sub-volt broadband hybrid plasmonic-vanadium dioxide switches. *Appl. Phys. Lett.* **2013**, *102*, doi:10.1063/1.4790834.
13. Markov, P.; Marvel, R.E.; Conley, H.J.; Miller, K.J.; Haglund, R.F.; Weiss, S.M. Optically monitored electrical switching in VO_2. *ACS Photonics* **2015**, *2*, 1175–1182.
14. Kruger, B.A.; Joushaghani, A.; Poon, J.K.S. Design of electrically driven hybrid vanadium dioxide (VO_2) plasmonic switches. *Opt. Express* **2012**, *20*, 23598–23609.
15. Jerominek, H.; Vincent, D.; Picard, F. Vanadium oxide films for optical switching and detection. *Opt. Eng.* **1993**, *32*, 2092–2099.
16. Briggs, R.M.; Pryce, I.M.; Atwater, H.A. Compact silicon photonic waveguide modulator based on the vanadium dioxide metal-insulator phase transition. *Opt. Express* **2010**, *18*, 11192–11201.
17. Sweatlock, L.A.; Diest, K. Vanadium dioxide based plasmonic modulators. *Opt. Express* **2012**, *20*, 8700–8709.
18. Hache, A.; Abdel Samad, B.; Chaker, M.; Herndaoui, A.; Vigne, S. Electro-optic switching of VO_2 for infrared spatial light modulation. In Proceedings of Optical Society of America, San Jose, CA, USA, 9–13 June 2013.
19. Ryckman, J.D.; Diez-Blanco, V.; Nag, J.; Marvel, R.E.; Choi, B.K.; Haglund, R.F.; Weiss, S.M. Photothermal optical modulation of ultra-compact hybrid Si-VO_2 ring resonators. *Opt. Express* **2012**, *20*, 13215–13225.
20. Cavalleri, A.; Toth, C.; Siders, C.W.; Squier, J.A.; Raksi, F.; Forget, P.; Kieffer, J.C. Femtosecond structural dynamics in VO_2 during an ultrafast solid-solid phase transition. *Phys. Rev. Lett.* **2001**, *87*, doi:10.1103/PhysRevLett.87.237401.
21. Liu, M.; Hwang, H.Y.; Tao, H.; Strikwerda, A.C.; Fan, K.; Keiser, G.R.; Sternbach, A.J.; West, K.G.; Kittiwatanakul, S.; Lu, J.; *et al.* Terahertz-field-induced insulator-to-metal transition in vanadium dioxide metamaterial. *Nature* **2012**, *487*, 345–348.
22. Nakano, M.; Shibuya, K.; Okuyama, D.; Hatano, T.; Ono, S.; Kawasaki, M.; Iwasa, Y.; Tokura, Y. Collective bulk carrier delocalization driven by electrostatic surface charge accumulation. *Nature* **2012**, *487*, 459–462.
23. Stefanovich, G.; Pergament, A.; Stefanovich, D. Electrical switching and Mott transition in VO_2. *J. Phys. Condens. Matter* **2000**, *12*, 8837–8845.
24. You, Z.; Xiao, N.C.; Chang, K.; Zheng, Y.; Mouli, C.; Ramanathan, S. Voltage-triggered ultrafast phase transition in vanadium dioxide Switches. *IEEE Elec. Dev. Lett.* **2013**, *34*, 220–222.
25. Driscoll, T.; Quinn, J.; Di Ventra, M.; Basov, D.N.; Seo, G.; Lee, Y.W.; Kim, H.T.; Smith, D.R. Current oscillations in vanadium dioxide: Evidence for electrically triggered percolation avalanches. *Phys. Rev. B* **2012**, *86*, doi:10.1103/PhysRevB.86.094203.
26. Appavoo, K.; Wang, B.; Brady, N.F.; Seo, M.; Nag, J.; Prasankumar, R.P.; Hilton, D.J.; Pantelides, S.T.; Haglund, R.F. Ultrafast phase transition via catastrophic phonon collapse driven by plasmonic hot-electron injection. *Nano Lett.* **2014**, *14*, 1127–1133.
27. Lysenko, S.; Vikhnin, V.; Rúa, A.; Fernández, F.; Liu, H. Critical behaviour and size effects in light-induced transition of nanostructured VO_2 films. *Phys. Rev. B* **2010**, *82*, doi:10.1103/PhysRevB.82.205425.

28. Joushaghani, A. Micro- and nano-scale optoelectronic devices using vanadium dioxide. Ph.D. Thesis, University of Toronto, Toronto, ON, Canada, 2014.
29. Kumar, S.; Pickett, M.D.; Strachan, J.P.; Gibson, G.; Nishi, Y.; Williams, R.S. Local temperature redistribution and structural transition during Joule-heating-driven conductance switching in VO_2. *Adv. Mater.* **2013**, *25*, 6128–6132.
30. Joushaghani, A.; Jeong, J.; Paradis, S.; Alain, D.; Stewart Aitchison, J.; Poon, J.K.S. Voltage-controlled switching and thermal effects in VO_2 nano-gap junctions. *Appl. Phys. Lett.* **2014**, *104*, doi:10.1063/1.4881155.
31. Joushaghani, A.; Jeong, J.; Paradis, S.; Alain, D.; Stewart Aitchison, J.; Poon, J.K.S. Electronic and thermal effects in the insulator-metal phase transition in VO_2 nano-gap junctions. *Appl. Phys. Lett.* **2014**, *105*, 231904; doi: 10.1063/1.4903806.
32. Zimmers, A.; Aigouy, L.; Mortier, M.; Sharoni, A.; Wang, S.; West, K.G.; Ramirez, J.G.; Schuller, I.K. Role of thermal heating on the voltage induced insulator-metal transition in VO_2. *Phys. Rev. Lett.* **2013**, *110*, doi:10.1103/PhysRevLett.110.056601.
33. Yang, Z.; Ko, C.; Balakrishnan, V.; Gopalakrishnan, G.; Ramanathan, S. Dielectric and carrier transport properties of vanadium dioxide thin films across the phase transition utilizing gated capacitor devices. *Phys. Rev. B* **2010**, *82*, doi:10.1103/PhysRevB.82.205101.
34. Ruzmetov, D.; Gopalakrishnan, G.; Ko, C.; Narayanamurti, V.; Ramanathan, S. Three-terminal field effect devices utilizing thin film vanadium oxide as the channel layer. *J. Appl. Phys.* **2010**, *107*, doi:10.1063/1.3408899.
35. Kim, H.T.; Kim, B.J.; Choi, S.; Chae, B.G.; Lee, Y.W.; Driscoll, T.; Qazilbash, M.M.; Basov, D.N. Electrical oscillations induced by the metal-insulator transition in VO_2. *J. Appl. Phys.* **2010**, *107*, doi:10.1063/1.3275575.
36. Ha, S.D.; Zhou, Y.; Fisher, C.J.; Ramanathan, S.; Treadway, J.P. Electrical switching dynamics and broadband microwave characteristics of VO_2 radio frequency devices. *J. Appl. Phys.* **2013**, *113*, doi:10.1063/1.4803688.
37. Aurelian, C.; Julien, G.; Jonathan, L.; David, M.; Corinne, C.; Jean-Christophe, O.; Alain, C.; Pierre, B. Voltage- and current-activated metal-insulator transition in VO_2-based electrical switches: A lifetime operation analysis. *Sci. Technol. Adv. Mater.* **2010**, *11*, doi:10.1088/1468-6996/11/6/065002.
38. Yong, Z.; Ji, H.; Chang, H.C.; Zhao, Y.F. Electrically controlled metal-insulator transition process in VO_2 thin films. *J. Phys. Condens. Matter* **2011**, *24*, doi:10.1088/0953-8984/24/3/035601.
39. Martens, K.; Radu, I.P.; Mertens, S.; Shi, X.; Nyns, L.; Cosemans, S.; Favia, P.; Bender, H.; Conard, T.; Schaekers, M.; *et al.* The VO_2 interface, the metal-insulator transition tunnel junction, and the metal-insulator transition switch On-Off resistance. *J. Appl. Phys.* **2012**, *112*, doi:10.1063/1.4767473.
40. Berglund, C. Thermal filaments in vanadium dioxide. *IEEE Trans. Electron. Devices* **1969**, *16*, 432–437.
41. Pergament, A.L.; Boriskov, P.P.; Velichko, A.A.; Kuldin, N.A. Switching effect and the metal-insulator transition in electric field. *J. Phys. Chem. Solids* **2010**, *71*, 874–879.

42. Oh, D.W.; Ko, C.; Ramanathan, S.; Cahill, D.G. Thermal conductivity and dynamic heat capacity across the metal-insulator transition in thin film VO_2. *Appl. Phys. Lett.* **2010**, *96*, doi:10.1063/1.3394016.
43. Neaman, D.A. *Semiconductor Physics and Devices: Basic Principles*; McGraw-Hill: New York, NY, USA, 2002.

© 2015 by the authors; licensee MDPI, Basel, Switzerland. This article is an open access article distributed under the terms and conditions of the Creative Commons Attribution license (http://creativecommons.org/licenses/by/4.0/).